Extracting correlation effects from momentum-resolved electron energy loss spectroscopy: Synergistic origin of the dispersion kink in $Bi_{2.1}Sr_{1.9}CaCu_2O_{8+x}$

Edwin W. Huang *
Department of Physics and Institute for Condensed Matter Theory, University of Illinois at Urbana-Champaign, Urbana, Illinois 61801, USA

Kridsanaphong Limtragool
Department of Physics, Faculty of Science, Mahasarakham University, Khamriang Sub-District, Kantharawichai District, Maha-Sarakham 44150, Thailand

Chandan Setty
Department of Physics, Rice University, Houston, Texas 77005, USA

Ali A. Husain
Department of Physics and Astronomy and Quantum Matter Institute, University of British Columbia, Vancouver, BC V6T 1Z4, Canada

Matteo Mitrano
Department of Physics, Harvard University, Cambridge, Massachusetts 02138, USA

Peter Abbamonte and Philip W. Phillips
Department of Physics, University of Illinois at Urbana–Champaign, Urbana, Illinois 61820, USA

(Received 6 October 2020; revised 20 December 2020; accepted 4 January 2021; published 15 January 2021)

We employ momentum-resolved electron energy loss spectroscopy (M-EELS) on $Bi_{2.1}Sr_{1.9}CaCu_2O_{8+x}$ to resolve the issue of the kink feature in the electron dispersion widely observed in the cuprates. To this end, we utilize the *GW* approximation to relate the density response function measured in M-EELS to the self-energy, isolating contributions from phonons, electrons, and the momentum dependence of the effective interaction to the decay rates. The phononic contributions, present in the M-EELS spectra due to electron-phonon coupling, lead to kink features in the corresponding single-particle spectra at energies between 40 and 80 meV, independent of the doping level. We find that a repulsive interaction constant in momentum space is able to yield the kink attributed to phonons in ARPES. Hence, our analysis of the M-EELS spectra points to local repulsive interactions as a factor that enhances the spectroscopic signatures of electron-phonon coupling in cuprates. We conclude that the strength of the kink feature in cuprates is determined by the *combined* action of electron-phonon coupling and electron-electron interactions.

DOI: 10.1103/PhysRevB.103.035121

I. INTRODUCTION

In strongly correlated electron matter, the noninteracting band dispersion fails to describe the elementary excitations. The departure from noninteracting physics is usually captured by the self-energy. It is in this context that the kinklike feature measured from angle-resolved photoemission spectroscopy (ARPES) [1–6] at 60 meV has risen to the fore as a telltale signature of a possibly universal energy scale in cuprate physics over a wide range of doping. Although phonons [6,7] are widely cited as the origin of the kink, there is good reason to believe that phonons alone are insufficient [8–13]. To help resolve this puzzle, we resort to momentum-resolved electron energy loss spectroscopy (M-EELS), which provides a measurement of the two-particle response or the density-density response function. Applying standard many-body approaches to the M-EELS data allows us to disentangle the many-body excitations encoded in the electron self-energy.

An advantage M-EELS has over ARPES is that because ARPES measures occupied states, extracting the self-energy from ARPES data relies on additional assumptions concerning the unoccupied spectral function, which may or may not be justified. A complementary approach to determining the self-energy from experimental data is to consider the scattering of electrons from bosonic fluctuations. Formally, two-particle response functions that characterize bosonic fluctuations can be related exactly to the single-particle self-energy via Hedin's equations [14]. This relationship allows one to identify features in the single-particle spectra with particular aspects of the two-particle spectra. To do so, we employ the *GW* approximation, which is based on assuming a

*edwinwhuang@gmail.com

bare vertex function in Hedin's equations. The self-energy is given in imaginary time by

$$\Sigma(\mathbf{k}, \tau) = \int \frac{d\mathbf{q}}{(2\pi)^2} G(\mathbf{k} - \mathbf{q}, \tau) W(\mathbf{q}, \tau + 0^+), \qquad (1)$$

where τ is imaginary time, G is the Green function, and

$$W(\mathbf{q}, \tau) = V(\mathbf{q})\delta(\tau) + V(\mathbf{q})\chi(\mathbf{q}, \tau)V(\mathbf{q}) \qquad (2)$$

is the screened Coulomb interaction, in terms of the bare Coulomb interaction $V(\mathbf{q})$ and the charge susceptibility $\chi(\mathbf{q}, \tau)$. In our calculations, the susceptibility will be taken directly from momentum-resolved electron energy loss spectroscopy (M-EELS) measurements of the density-density response function in the high-T_c cuprate $Bi_{2.1}Sr_{1.9}CaCu_2O_{8+x}$ (BSCCO). This recently developed technique [15] provides reliable measurements of the total density response of a system for momenta throughout the Brillouin zone with meV resolution. Moreover, unlike other probes (like inelastic x-ray scattering), the density response of M-EELS primarily originates from valence electrons and shields out contributions from the core states. Equipped with experimental knowledge of the density response of valence electrons for all frequencies and momenta, we undertake the tasks of determining the corresponding self-energy and examining to what extent the results agree with other known probes of the self-energy.

In this paper, we showcase how M-EELS can be used as a purely nonoptical probe of correlation effects captured in the momentum- and frequency-dependent scattering rate or self-energy. Using the density response measured in M-EELS [16–18], we employ the *GW* method to evaluate the self-energy for the under-, optimally, and overdoped copper oxide superconductor $Bi_{2.1}Sr_{1.9}CaCu_2O_{8+x}$. In the process, we isolate the contributions from phonons as a cause of the kink in the energy dispersion in the momentum- and energy-dependent curves as seen in ARPES. Hence, we are able to offer new insights into the origin of the debated kink features around ∼60 meV [1–6]. Our calculations find that, independent of doping, kinks appear at the energies of the phonons visible by M-EELS when considering effective electron interactions that are local in real space.

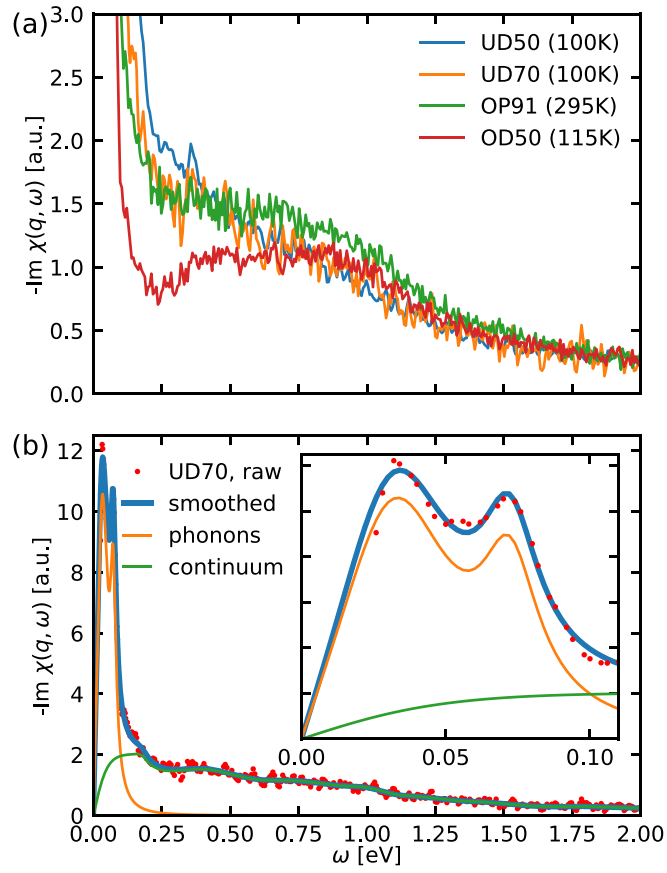

FIG. 1. (a) Plots of the imaginary part of the density-density response function at momentum $q = (0.5, 0)$ in r.l.u., as measured by M-EELS for four dopings of BSCCO. (b) Separation of the M-EELS data for UD70 into phonon peaks (orange curve) and the electronic continuum (green curve), which add to form the smoothed curve (blue). The phonon peaks are fitted with two antisymmetrized Lorentzians, although they may consist of more than two phonons that are not resolved. The smoothed curve is obtained by a smoothed spline fit to the raw data (red dots). Inset: Same plot at low frequencies. Data below 20 meV are contaminated by the tails of the strong quasielastic peak.

II. PRELIMINARIES

The imaginary part of the density response function, $\chi''(\mathbf{q}, \omega)$, in BSCCO can be measured using M-EELS as reported in [16–18]. In this paper, we use $\chi''(\mathbf{q}, \omega)$ measured in BSCCO at four doping concentrations to compute the imaginary part of the self-energy. The four dopings include underdoping with $T_c = 50$ K and $T_c = 70$ K, optimal doping with $T_c = 91$ K, and overdoping with $T_c = 50$ K. In Fig. 1, we display $\chi''(\mathbf{q}, \omega)$ for all four dopings at fixed $q = 0.5$ reciprocal lattice units (r.l.u.) to demonstrate the doping dependence of features in χ''. As shown in Fig. 1(b), these include two phonon peaks at energies of about 40 and 70 meV and a broader electronic continuum with an edge at about 1 eV. Compared to the flat background from 100 meV to 1 eV in the optimally doped case, there is a suppression (an enhancement) of χ'' at about 200–400 meV in the overdoped (underdoped) case.

We assume that $\chi''(\mathbf{q}, \omega)$ does not depend on the direction of $\mathbf{q}$, i.e., $\chi''(\mathbf{q}, \omega) = \chi''(q, \omega)$. Figure S2B in Ref. [17] showed that $\chi''(\mathbf{q}, \omega)$ measured along the nodal and antinodal directions coincide for $q \equiv |\mathbf{q}|$ between 0.1 and 0.5 r.l.u. For smaller values of $q \approx 0.05$ r.l.u., there is a difference between χ'' in the two directions at energies below 1 eV. For simplicity of the calculations, we ignore this deviation at small q and take $\chi''(\mathbf{q}, \omega) = \chi''(q, \omega)$ for all $\mathbf{q}$ in the Brillouin zone. A full map of the Brillouin zone by M-EELS may be of interest in future studies to address the validity of this approximation.

To obtain the screened interaction W from the density response χ, a concrete form for the electron interaction, $V(q)$, is required. Reference [17] considered the susceptibility $\chi(q, \omega)$ in terms of the background susceptibility ε_∞ (4.5 for BSCCO [19]) and polarizability $\Pi(q, \omega)$,

$$\chi(q, \omega) = \frac{\Pi(q, \omega)}{\varepsilon_\infty - V(q)\Pi(q, \omega)}, \qquad (3)$$

and found that the imaginary part of the polarizability factors in momentum and energy with the form (for optimal doping)

$$\Pi''(q,\omega) = -\Pi_0(q)\tanh\frac{\omega_c^2(q)}{\omega^2} \tag{4}$$

if the effective interaction is given by

$$V(q) = V_0\frac{\exp(-zq)}{q}, \tag{5}$$

where $V_0 = 820$ eV Å^3 and $z = 14.3$ Å. The prefactor function $\Pi_0(q) \propto q^2$ and the cutoff frequency $\omega_c(q) \approx 1$ eV. The specific form of $V(q)$ here is not determined directly and is not physically motivated. chosen based on a fit of the data to (4). Notably, even by this scheme, the value of $V(q)$ for large q is not strongly constrained.

We therefore consider also $V(q)$ with a more regular momentum dependence. Specifically, we study the simplest case in which $V(q) \propto 1$, corresponding to a local real-space interaction. One of our main conclusions is that while $V(q)$ as given in (5) leads to factorizability of $\Pi(\mathbf{q},\omega)$, it does not produce the expected behavior of the kink in the spectral function $A(\mathbf{k},\omega)$ in our calculations.

For the band structure, we include up to next-next-nearest-neighbor hoppings, t, t', and t'':

$$\begin{aligned}\epsilon_{\mathbf{k}} =& -2t(\cos(k_x a)+\cos(k_y a)) - 4t'\cos(k_x a)\cos(k_y a)\\ &- 2t''(\cos(2k_x a)+\cos(2k_y a)).\end{aligned} \tag{6}$$

The hoppings we use in this paper are $t = 0.42$ eV, $t' = -0.110$ eV, and $t'' = 0.055$ eV [20,21]. The lattice parameter is $a = 3.81$ Å [17].

One of our goals is to separate and isolate the contributions from phonons and from the electronic background to the self-energy. To this end, we fit the two phonon peaks at energies of about 40 and 70 meV with two Lorentzian functions [antisymmetrized to obey $\chi''(\mathbf{q},-\omega) = -\chi''(\mathbf{q},\omega)$]. These peaks may be subtracted from the data to obtain the electronic continuum, as shown in Fig. 1(b). We then compute the imaginary part of the self-energy from the density response considering only the phonons peaks, only the electronic continuum, or the entire spectrum. Plugging in the self-energy to Dyson's equation yields the Green function, from which we plot the spectral function and visualize the dispersion by looking at the maxima of momentum distribution curves (MDCs), as is commonly done to analyze ARPES data.

As is evident from Eq. (2), there are two contributions to the self-energy. The first term, which contains only the bare interaction, is frequency independent and hence just provides a shift to the band dispersion. This term is dropped in our calculations to avoid double-counting, since our noninteracting dispersion, (6), was determined by a fit to experimental ARPES data, which of course include the effects of screening. The frequency dependence of the self-energy arises entirely from the second term that includes the density-density response. Then, in real frequency, (1) takes the form

$$\begin{aligned}\Sigma''(\mathbf{k},\omega) =& \int\frac{d\mathbf{q}}{(2\pi)^2}d\Omega V(\mathbf{q})^2[f(-\Omega)+n(\omega-\Omega)]\\ &\times\frac{-1}{\pi}G''(\mathbf{k}-\mathbf{q},\Omega)\chi''(\mathbf{q},\omega-\Omega),\end{aligned} \tag{7}$$

where $f(\omega)$ and $n(\omega)$ are the Fermi and Bose distribution functions, respectively, and Σ, G, and χ are understood to be evaluated with an infinitesimal displacement above the real frequency axis. For numerical stability, we perform all calculations with a small finite amount γ above the real frequency axis rather than using Eq. (7). Following the methods in [22], $\Sigma(\mathbf{k},\omega+i\gamma)$ can be evaluated efficiently via fast Fourier transforms in terms of G and χ using

$$\begin{aligned}\Sigma(\mathbf{r},\omega+i\gamma) =& \int_0^\infty dt\,\Sigma(\mathbf{r},t)e^{i(\omega+i\gamma)t}\\ \Sigma(\mathbf{r},t) =& i2\pi T\Re\widetilde{\chi}(\mathbf{r},0+i0^+)e^{\gamma t}\rho(\mathbf{r},t)\\ &- i(2\pi)^2\nu(\mathbf{r},t)\big(\mathcal{A}(\mathbf{r},t)+\mathcal{A}(\mathbf{r},-t)^*e^{2\gamma t}\big)\\ &+ i(2\pi)^2\rho(\mathbf{r},t)(\mathcal{B}(\mathbf{r},t)^*+\mathcal{B}(\mathbf{r},-t))e^{2\gamma t}\end{aligned} \tag{8}$$

with

$$\begin{aligned}\rho(\mathbf{r},t) &= \int_{-\infty}^{\infty}\frac{d\omega}{2\pi}e^{-i\omega t}\frac{-1}{\pi}G''(\mathbf{r},\omega+i\gamma),\\ \mathcal{A}(\mathbf{r},t) &= \frac{i}{2\pi}\int_{-\infty}^{\infty}\frac{d\omega}{2\pi}e^{-i\omega t}f(\omega+i\gamma)^*G(\mathbf{r},\omega+i\gamma)^*,\\ \nu(\mathbf{r},t) &= \int_{-\infty}^{\infty}\frac{d\omega}{2\pi}e^{-i\omega t}\frac{-1}{\pi}\widetilde{\chi}''(\mathbf{r},\omega+i\gamma),\\ \mathcal{B}(\mathbf{r},t) &= \frac{i}{2\pi}\int_{-\infty}^{\infty}\frac{d\omega}{2\pi}e^{-i\omega t}n(\omega+i\gamma)^*\widetilde{\chi}(\mathbf{r},-\omega+i\gamma),\\ \widetilde{\chi}(\mathbf{r},\omega) &= \frac{1}{N}\sum_{\mathbf{q}}e^{i\mathbf{q}\cdot\mathbf{r}}V(\mathbf{q})^2\chi(\mathbf{q},\omega).\end{aligned} \tag{9}$$

All momentum integrals are discretized on a grid of size $N = 200\times200$. Frequency integrals are discretized with steps of 0.002 eV in the range $[-12$ eV, 12 eV$]$. We have checked that increasing the density of the momentum and frequency grids and extending the range of the frequency integration do not affect our results. In the Fermi and Bose distribution functions, we have assumed a temperature of $T = 0.002$ eV. As this value is smaller than the lowest accessible energy of the M-EELS spectra ($\sim$20 meV due to quasielastic tails), varying it does not affect our results. Finally, the parameter γ must satisfy $\gamma < \pi T/2$ as discussed in [22]. We found $\gamma = \pi T/3$ to yield numerically stable results.

The calculation of the self-energy begins by using a noninteracting Green function, $G(\mathbf{k},\omega+i\gamma) = [\omega+i\gamma-\epsilon_{\mathbf{k}}]^{-1}$. After a Fourier transform to real space, Eqs. (8) and (9) are used to evaluate $\Sigma(\mathbf{r},\omega+i\gamma)$, which is then transformed back into momentum space. A new Green function is obtained via

$$G(\mathbf{k},\omega+i\gamma) = \frac{1}{\omega+i\gamma-\epsilon_{\mathbf{k}}-\Sigma(\mathbf{k},\omega+i\gamma)} \tag{10}$$

and may be used as the new input to the calculation. This procedure may be stopped after the first calculation, which we refer to as the one-loop calculation (similarly to Ref. [16]), or repeated until the self-energy and Green function converge, i.e., self-consistently. Typically, self-consistency is achieved within $\sim$10 iterations.

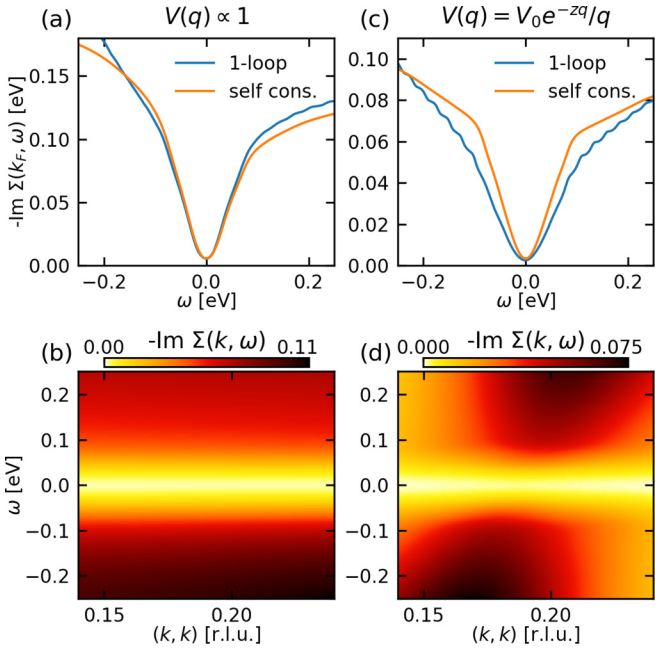

FIG. 2. Plots of the imaginary part of the self-energy in the nodal direction computed by the *GW* approximation with M-EELS data for underdoped BSCCO ($T_c = 70$ K). (a), (b) Computed using $V(q) \propto 1$; (c), (d) computed using Eq. (5). Both (b) and (d) are two-dimensional plots of the self-consistent calculation in which the color shows the magnitude of the imaginary part of the self-energy along a nodal cut. Darker colors correspond to a higher intensity.

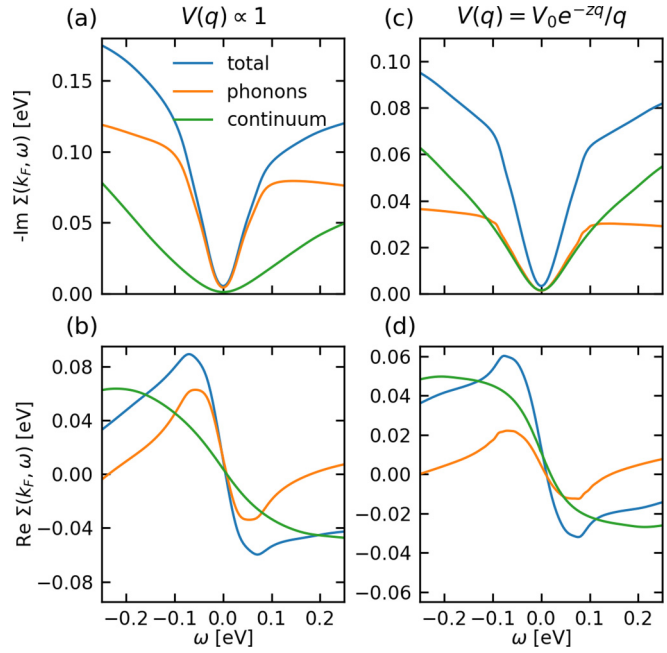

FIG. 3. Imaginary (a), (c) and real (b), (d) parts of the self-energy for UD70 BSCCO at the nodal k_F. (a), (b) Computed using $V(q) \propto 1$; (c), (d) computed using Eq. (5). Different curves correspond to using all of the M-EELS data (blue), keeping only the phonon peaks (orange), and keeping only the electronic continuum (green).

III. RESULTS

We numerically calculated the real and imaginary parts of the self-energy using Eqs. (8) and (9). Figures 2(a) and 2(c) compare the self-consistent and one-loop evaluations of the imaginary part of the self-energy for two kinds of interaction potentials, a constant, $V(q) \approx 1$, and the form $V(q) = V_0 e^{-zq}/q$ as discussed in Refs. [17] and [18]. The one-loop self-energies show minor oscillations due to the finite 200×200 momentum grid; these artifacts go away with increasing momentum resolution and hence can be ignored. While the self-consistent solution and the one-loop calculation exhibit somewhat different slopes at high energy, the behavior at low energies is qualitatively similar. In the subsequent calculations, we do not find major differences between the two schemes, and we focus on data from the self-consistent calculations.

We see also that the two forms of potentials $V(q)$ yield quite similar imaginary parts of the self-energies, which is surprising given that one is constant and the other is sharply peaked as functions of q. However, as we see, this agreement is misleading, as significant changes will become apparent in our evaluation of the spectral function and dispersion curves. Figures 2(b) and 2(d) show a two-dimensional color plot of $\Sigma''(\mathbf{k}, \omega)$ as a function of both the frequency and the momentum, as obtained from the self-consistent calculation. As expected, the momentum dependence of the self-energy is stronger for the momentum-dependent interaction potential. What our analysis shows thus far is that we have a numerically self-consistent stable method to calculate the self-energy and analyze the results for an arbitrary potential that goes beyond the one-loop approximation used previously [16].

For BSCCO UD70, we now analyze the role the two distinct parts of the susceptibility [Fig. 1(b)] play in the self-energy. Figure 3 displays both the real and the imaginary parts of the self-energy. In the orange curves, the calculation uses only the phonon peaks, and in the green curves, the calculation uses only the electronic continuum. The real part of the self-energy exhibits a distinct nonmonotonic behavior. We find that the 40- and 70-meV phonon peaks in the susceptibility correspond to a broad maximum and minimum at ∼±60 meV in the real part of the self-energy and a corresponding change in slope in the imaginary part. This behavior will be linked to the kink feature in the energy dispersion curves. When only the electronic continuum is included, there is no particular frequency scale visible in the range [−0.2 eV, 0.2 eV]. As is evident in Fig. 3, the qualitative aspects of these trends appear independent of the details of the interaction potential. However, as we see in studying the spectral function, the relative ratio of the contributions of the phonons and electronic continuum is affected by the choice of the interaction potential, which has significant consequences.

We are now set to address our key problem of the necessary ingredients to obtain the kink feature reported in previous ARPES studies on the cuprates [6,23,24]. Figure 4 contains plots of the spectral function $A(\mathbf{k}, \omega)$ as two-dimensional plots of frequency and momentum. To visualize the dispersion, we also plot the noninteracting dispersion (dashed lines) and the locus of maximal intensity along cuts of constant energy, i.e., MDC maxima (solid lines). Figures 4(a)–4(c) show the spectral functions and MDC maxima from calculations using

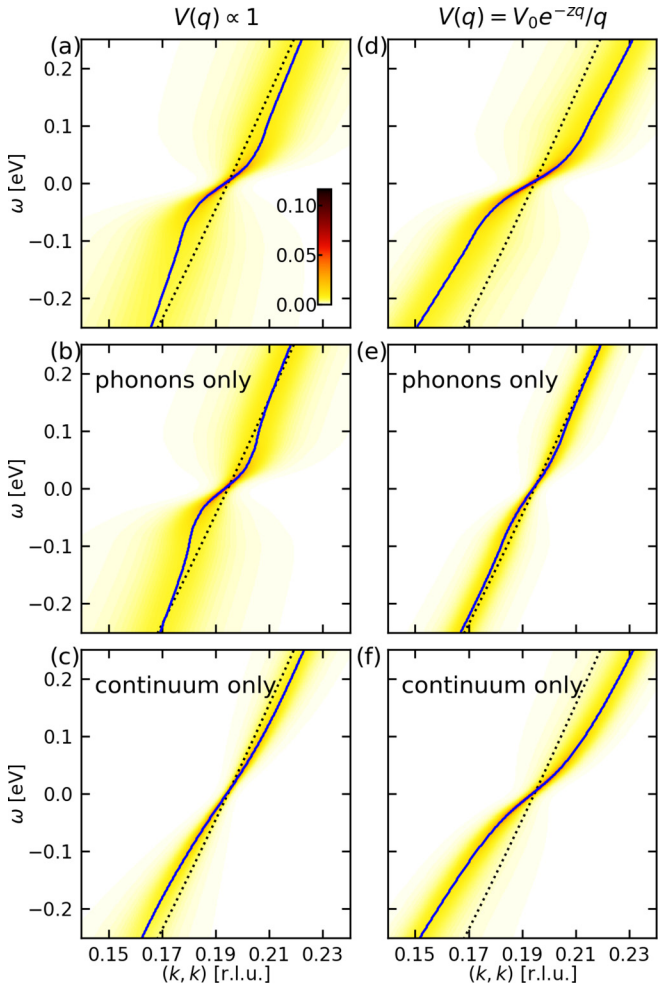

FIG. 4. Spectral functions as functions of the momentum and energy. Solid lines represent maxima of the momentum distribution curves (MDCs). Dashed lines show the noninteracting dispersion. Computed for a constant potential with the full self-energy (a), just the phonons (b), and just the electronic continuum (c). The same as (d)–(f), but for the potential as shown.

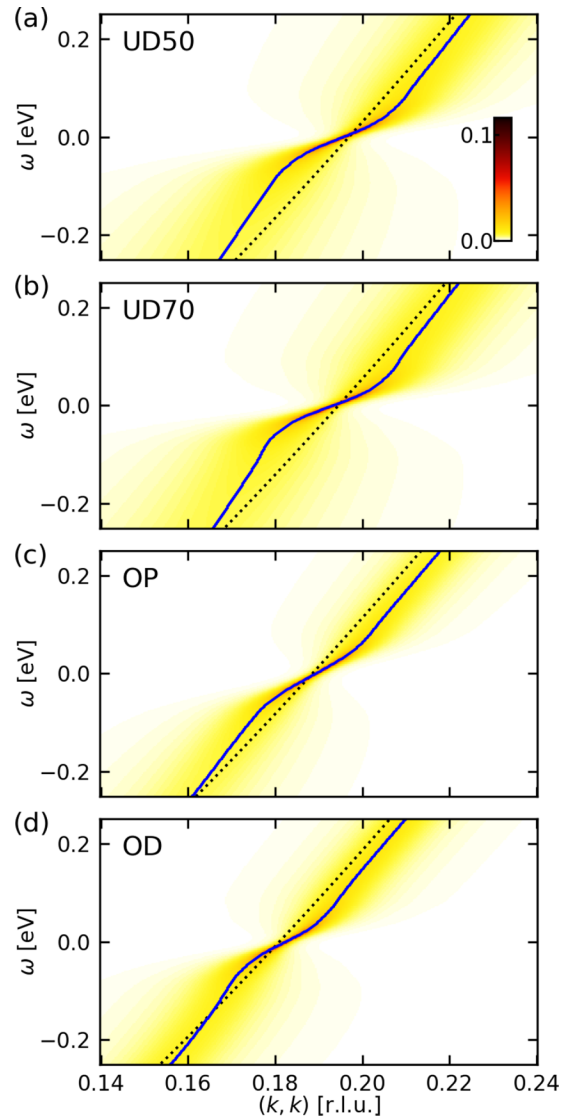

FIG. 5. Spectral functions (color) and MDC maxima (solid line) calculated using the constant potential, $V(\mathbf{q}) \propto 1$, for different doping. Doping levels are as labeled: (a) UD50, (b) UD70, (c) optimal doping (OP), and (d) overdoping (OD).

a momentum-independent potential. As is evident, the kink feature present in Fig. 4(a) is lost completely when only the electronic continuum feature is retained. When phonons are present, there are clearly kinks at $\sim\pm 60$ meV as Figs. 4(a) and 4(b) demonstrate. This is clearly correlated with the minimum and maximum in the real part of the self-energy as discussed in Fig. 3. As seen experimentally [6,23,24], the kink feature involves a renormalization of the band for $|\omega| \sim 60$ meV that sharply connects back to the unrenormalized noninteracting band at higher energies. Such behavior is absent for the strongly momentum-dependent potential. While there is a renormalization of the dispersion at low frequencies in Fig. 4(d), there is no connection back to the noninteracting band. By analyzing the spectra when only phonons are kept [Fig. 4(e)], we see that the phonons affect the dispersion minimally for the given form of the momentum-dependent interaction. Therefore, the renormalization in Fig. 4(d) derives almost entirely from the contribution of the electronic continuum [Fig. 4(f)], which has no clearly defined energy scale. While there is an apparent change in the renormalization in Fig. 4(d) around roughly 30 meV, this is not related to any feature in $\chi(\mathbf{q}, \omega)$ but rather controlled by the magnitude of V_0. (For the momentum-dependent interaction, changing this prefactor strongly affects the range where the dispersion is renormalized, in contrast to the momentum-independent interaction, where the energies of the features are set by the energies of the phonon peaks.)

The doping dependence of the spectral function is shown in Fig. 5. In these calculations, we have used a momentum-independent interaction and the full density response, including both the phonons and the electronic continuum. The same kink behavior discussed previously persists in the dispersion for all doping levels, though it is strongest in the underdoped samples.

The crucial effect of doping on the imaginary part of the density response is the supression or enhancement of

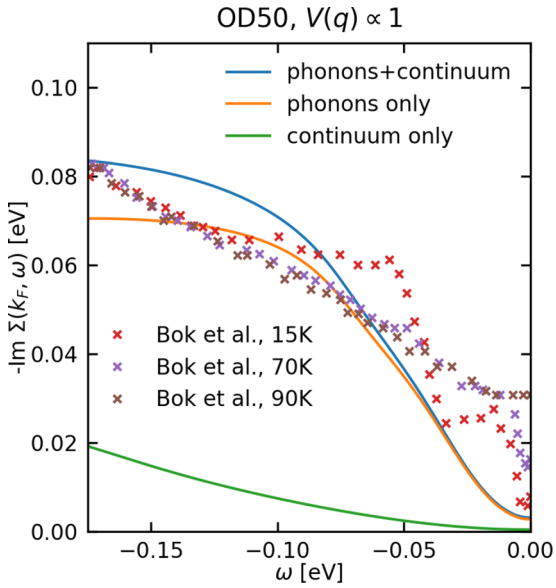

FIG. 6. Comparison plots between the imaginary part of the self-energy at nodal k_F obtained in this work and from ARPES for overdoped BSCCO [28]. The T_c of the overdoped sample of Bok *et al.* is 82 K.

spectral weight at energies $\lesssim$0.5 eV. Relative to optimal doping, the intensity is suppressed around ∼0.3 eV for overdoped samples and enhanced in underdoped samples [Fig. 1(a)]. This low-energy enhancement of the susceptibility does not significantly affect the calculated spectra and the kink around 60 meV remains essentially intact.

Comparisons of the self-energy as obtained from ARPES and scattering rates from optical probes such as FTIR and ellipsometry have been made previously [1–3,25]. The contribution of magnetic excitations as probed by neutron and Raman scattering [26,27] has also been considered in calculations of the self-energy and discussions of the origin of the kink [11]. Our results derived from M-EELS data with momentum dependence provide a new perspective by analyzing the electronic self-energy due to charge fluctuations. Figure 6 plots a comparison between the imaginary parts of the self-energies obtained from our M-EELS data and ARPES [28]. The imaginary part of the self-energy from M-EELS with the constant potential has a similar magnitude and general frequency dependence as those extracted from ARPES [28], indicating that we have chosen an appropriate strength for the interaction potential. Once again, we show that modeling with just the electronic continuum fails to account for the sharp rise from $\omega = 0$ of the self-energy. This behavior can be accounted for by including just the phonon part, although this contribution is peaked at $\omega = 0$. Hence, our work on extracting the self-energy from M-EELS concurs with the ARPES work that phonons are the origin [6,7,29] of the kink feature at 60 meV. While we cannot rule out other mechanisms, our work strongly suggests that phonons are sufficient to achieve a low-energy kinklike feature. Moreover, since these features occur above T_c, they appear not to be dependent on superconductivity, consistent with the existing literature [1].

IV. FINAL REMARKS

Since M-EELS is inherently a two-particle probe, it provides direct information regarding the form of the electron-electron interaction. We have found that consilience with the kink feature in ARPES requires an interaction broad in momentum space, implying the presence and importance of short-range and local repulsive interactions. Because the analysis leading to (5) does not strongly constrain the form of the interaction at large momenta, our result is not necessarily in contradiction with the finding that the polarizability factors in the momentum and frequency, as demonstrated in (4).

Local and short-ranged interactions are at the heart of the theoretical challenges associated with studying cuprates. Strong repulsion [30,31] is the origin of the Mott insulating behavior in the parent compounds and also certainly responsible for many, if not most, of the complex behavior in the doped compounds. We have shown here that these interactions are also crucial to the behavior of kinks in the single-particle dispersion, even though their existence and energy scale are tied to bosonic modes, which we identify as phonons in our M-EELS data.

Kinks due to electron-phonon coupling are typically considered in models [29] with only electron-phonon interactions. Such models display kinks in their spectra if the interactions are short-ranged or local as in, for instance, the Holstein model. (This may be contrasted, for instance, with electron-phonon interactions with forward scattering concentrated near $\mathbf{q} = 0$, which instead lead to replica bands [32]). In the framework of the calculations in our work, these models may be understood by integrating out the phonons, leading to an effective retarded electron-electron interaction that is short-ranged and attractive. This retarded interaction gives a frequency dependence to the first term in (2), and since it contains poles at the phonon frequencies, it also yields a contribution to the self-energy that forms dispersion kinks provided the interaction is sufficiently local as we have discussed.

The Mott insulating nature of parent compound cuprates implies that the Coulombic (repulsive) electron-electron interactions significantly overcome the effective attractive interactions due to electron-phonon coupling. However, the frequency dependence of the total effective interaction remains unchanged by including repulsion, and so the first term in (2) contributes to the self-energy in the same way as in a model with only electron-phonon coupling. In our simple calculations, we do not model the frequency dependence of $V(\mathbf{q})$. Yet we find that the self-energy due to the second term in (2) alone, as in our calculations, can also lead to a substantial kink feature in $A(k, \omega)$. In this second term, the instantaneous repulsive electron-electron interactions in $V(\mathbf{q})$ leads to kinks because of the frequency dependence of $\chi(q, \omega)$. Here, significant electron-phonon coupling is still necessary for the susceptibility to display phonon peaks as seen in the M-EELS data. The importance of all of these factors leads us to conclude that *the strength of the kink feature in cuprates reflects the combined effects of strongly repulsive electron-electron interactions and electron-phonon coupling*. Such a synergistic effect has been discussed, in a different context, as a feedback loop that potentially enhances superconductivity [33].

The strengthening effect of repulsive electron-electron interactions on the dispersion kink may provide a possible resolution of *ab initio* calculations that have found electron-phonon coupling in cuprates to be too weak, on its own, to account for the kink observed in ARPES [8]. This effect may also be tested in simulations of microscopic lattice models involving both electron-electron and electron-phonon interactions such as the Hubbard-Holstein model. Semianalytical diagrammatic methods similar to the *GW* approximation used here and Migdal-Eliashberg calculations for electron-phonon models are a possible approach. We have seen that these methods are well capable of characterizing the renormalization of the dispersion that leads to the kink feature. However, we caution that such calculations do not do full justice to the strongly repulsive interactions in the cuprates. This may be seen by considering the self-energy for Mott insulators and doped Mott insulators. The simple Hatsugai-Kohmoto model [31] provides a clear example. In this model, a local interaction in momentum space yields the Mott physics. The single-particle dispersion, which can be solved for exactly, is modified from the noninteracting ϵ_k, to $\epsilon_k + U/2 - \Sigma(k, \omega)$, to the form

$$\Sigma(k, \omega) = \frac{(U/2)^2}{\omega + i0^+ - (\epsilon_k - \mu + U/2)} \tag{11}$$

at half-filling [34]. As is evident, the self-energy contains a pole at $\omega = 0$, the key feature of Mottness [30] that leads to the formation of upper and lower Hubbard bands. This divergence of the self-energy cannot be captured via perturbative techniques. Therefore, we believe that nonperturbative many-body techniques and models that treat electron-electron and electron-phonon interactions on equal footing [35,36], while challenging, are ultimately necessary to capture the full richness of cuprate phenomenology and, in particular, the detailed behavior of dispersion kinks.

ACKNOWLEDGMENTS

E.W.H. was supported by the Gordon and Betty Moore Foundation EPiQS Initiative through Grants No. GBMF 4305 and No. GBMF 8691. P.A. and P.W.P. acknowledge support from Quantum Sensing and Quantum Materials, an Energy Frontier Research Center funded by the U.S. Department of Energy, Office of Science, Basic Energy Sciences, under Award No. DE-SC0021238. P.W.P. also thanks the NSF for partial funding of this project under Grant No. DMR-1919143. C.S. was supported by DOE Grant No. DE-FG02-05ER46236.

[1] A. Damascelli, Z. Hussain, and Z.-X. Shen, Rev. Mod. Phys. **75**, 473 (2003).
[2] A. Kaminski, J. Mesot, H. Fretwell, J. C. Campuzano, M. R. Norman, M. Randeria, H. Ding, T. Sato, T. Takahashi, T. Mochiku, K. Kadowaki, and H. Hoechst, Phys. Rev. Lett. **84**, 1788 (2000).
[3] A. Puchkov, D. Basov, and T. Timusk, J. Phys.: Condens. Matter **8**, 10049 (1996).
[4] J. Hwang, E. J. Nicol, T. Timusk, A. Knigavko, and J. P. Carbotte, Phys. Rev. Lett. **98**, 207002 (2007).
[5] J. Hwang, T. Timusk, and G. D. Gu, Nature **427**, 714 (2004).
[6] A. Lanzara, P. V. Bogdanov, X. J. Zhou, S. A. Kellar, D. L. Feng, E. D. Lu, T. Yoshida, H. Eisaki, A. Fujimori, K. Kishio, J.-I. Shimoyama, T. Noda, S. Uchida, Z. Hussain, and Z.-X. Shen, Nature **412**, 510 (2001).
[7] W. Meevasana, N. J. C. Ingle, D. H. Lu, J. R. Shi, F. Baumberger, K. M. Shen, W. S. Lee, T. Cuk, H. Eisaki, T. P. Devereaux, N. Nagaosa, J. Zaanen, and Z.-X. Shen, Phys. Rev. Lett. **96**, 157003 (2006).
[8] F. Giustino, M. L. Cohen, and S. G. Louie, Nature **452**, 975 (2008).
[9] A. V. Chubukov and M. R. Norman, Phys. Rev. B **70**, 174505 (2004).
[10] A. A. Kordyuk, S. V. Borisenko, V. B. Zabolotnyy, J. Geck, M. Knupfer, J. Fink, B. Büchner, C. T. Lin, B. Keimer, H. Berger, A. V. Pan, S. Komiya, and Y. Ando, Phys. Rev. Lett. **97**, 017002 (2006).
[11] T. Dahm, V. Hinkov, S. V. Borisenko, A. A. Kordyuk, V. B. Zabolotnyy, J. Fink, B. Büchner, D. J. Scalapino, W. Hanke, and B. Keimer, Nat. Phys. **5**, 217 (2019).
[12] C. Raas, P. Grete, and G. S. Uhrig, Phys. Rev. Lett. **102**, 076406 (2009).
[13] K. Matsuyama, E. Perepelitsky, and B. S. Shastry, Phys. Rev. B **95**, 165435 (2017).
[14] L. Hedin, Phys. Rev. **139**, A796 (1965).
[15] R. Egerton, Ultramicroscopy **107**, 575 (2007).
[16] S. Vig, A. Kogar, M. Mitrano, A. A. Husain, V. Mishra, M. S. Rak, L. Venema, P. D. Johnson, G. D. Gu, E. Fradkin, M. R. Norman, and P. Abbamonte, SciPost Phys. **3**, 026 (2017).
[17] M. Mitrano, A. A. Husain, S. Vig, A. Kogar, M. S. Rak, S. I. Rubeck, J. Schmalian, B. Uchoa, J. Schneeloch, R. Zhong, G. D. Gu, and P. Abbamonte, Proc. Natl. Acad. Sci. USA **115**, 5392 (2018).
[18] A. A. Husain, M. Mitrano, M. S. Rak, S. Rubeck, B. Uchoa, K. March, C. Dwyer, J. Schneeloch, R. Zhong, G. D. Gu, and P. Abbamonte, Phys. Rev. X **9**, 041062 (2019).
[19] J. Levallois, M. K. Tran, D. Pouliot, C. N. Presura, L. H. Greene, J. N. Eckstein, J. Uccelli, E. Giannini, G. D. Gu, A. J. Leggett, and D. van der Marel, Phys. Rev. X **6**, 031027 (2016).
[20] E. Pavarini, I. Dasgupta, T. Saha-Dasgupta, O. Jepsen, and O. K. Andersen, Phys. Rev. Lett. **87**, 047003 (2001).
[21] R. S. Markiewicz, S. Sahrakorpi, M. Lindroos, H. Lin, and A. Bansil, Phys. Rev. B **72**, 054519 (2005).
[22] J. Schmalian, M. Langer, S. Grabowski, and K. Bennemann, Comput. Phys. Commun. **93**, 141 (1996).
[23] H. Anzai, M. Arita, H. Namatame, M. Taniguchi, M. Ishikado, K. Fujita, S. Ishida, S. Uchida, and A. Ino, Sci. Rep. **7**, 4830 (2017).
[24] S. A. Sreedhar, A. Rossi, J. Nayak, Z. W. Anderson, Y. Tang, B. Gregory, M. Hashimoto, D.-H. Lu, E. Rotenberg, R. J. Birgeneau, M. Greven, M. Yi, and I. M. Vishik, Phys. Rev. B **102**, 205109 (2020).
[25] D. N. Basov and T. Timusk, Rev. Mod. Phys. **77**, 721 (2005).
[26] T. P. Devereaux and R. Hackl, Rev. Mod. Phys. **79**, 175 (2007).

[27] R. Zeyher and A. Greco, Phys. Rev. B **87**, 224511 (2013).
[28] J. M. Bok, J. J. Bae, H.-Y. Choi, C. M. Varma, W. Zhang, J. He, Y. Zhang, L. Yu, and X. J. Zhou, Sci. Adv. **2**, e1501329 (2016).
[29] S. Johnston, F. Vernay, B. Moritz, Z.-X. Shen, N. Nagaosa, J. Zaanen, and T. P. Devereaux, Phys. Rev. B **82**, 064513 (2010).
[30] P. Phillips, Rev. Mod. Phys. **82**, 1719 (2010).
[31] D. Lidsky, J. Shiraishi, Y. Hatsugai, and M. Kohmoto, Phys. Rev. B **57**, 1340 (1998).
[32] J. J. Lee, F. T. Schmitt, R. G. Moore, S. Johnston, Y.-T. Cui, W. Li, M. Yi, Z. K. Liu, M. Hashimoto, Y. Zhang, D. H. Lu, T. P. Devereaux, D.-H. Lee, and Z.-X. Shen, Nature **515**, 245 (2014).
[33] Y. He, M. Hashimoto, D. Song, S.-D. Chen, J. He, I. M. Vishik, B. Moritz, D.-H. Lee, N. Nagaosa, J. Zaanen, T. P. Devereaux, Y. Yoshida, H. Eisaki, D. H. Lu, and Z.-X. Shen, Science **362**, 62 (2018).
[34] P. W. Phillips, L. Yeo, and E. W. Huang, Nat. Phys. **16**, 1175 (2020).
[35] S. Johnston, E. A. Nowadnick, Y. F. Kung, B. Moritz, R. T. Scalettar, and T. P. Devereaux, Phys. Rev. B **87**, 235133 (2013).
[36] C. B. Mendl, E. A. Nowadnick, E. W. Huang, S. Johnston, B. Moritz, and T. P. Devereaux, Phys. Rev. B **96**, 205141 (2017).